ChemComm

COMMUNICATION

View Article Online
View Journal



Cite this: DOI: 10.1039/d6cc01363e

Received 6th March 2026,
Accepted 28th May 2026

DOI: 10.1039/d6cc01363e

rsc.li/chemcomm

# Template-guided sodium intercalation enables phase-pure alkali metal-based ternary chalcogenides nanocrystals

Niraj Nitish Patil, * Hannah McKeever, Monika Ahlawat, Kevin M Ryan and Shalini Singh *



**Alkali metal-based ternary chalcogenides are promising materials which remain synthetically underexplored. Here, a template-based strategy enables synthesis of colloidal $NaInS_2$ and $NaIn_3Se_5$ nanocrystals. Mechanistic insights reveal sodium intercalation as a predictive route to phase-pure ABZ nanocrystals.**

Chalcogenide materials have attracted considerable attention owing to their diverse applications in energy storage and conversion.[1,2] Within this broad class, alkali metal-based ternary chalcogenides, commonly referred to as ABZ materials, where A = alkali metal, B = transition metal, Z = chalcogen, are promising emerging candidates for functional energy materials.[3–9] Their diverse crystal structures, tunable functionalities and ability to be engineered as inorganic semiconductors make them attractive for a wide range of applications.[10–15] Despite their promise, the synthesis of ABZ nanomaterials (NMs) remains a central challenge. Traditional synthetic protocols rely on a trial-and-error approach, guided by factors such as precursor reactivities, molar ratios, decomposition temperatures, and growth times to achieve phase-pure products. While effective in many cases, this strategy is time-consuming and constrained by the disparate chemical reactivities and kinetics across different elemental combinations.[5] Synthetic protocols developed for one ABZ composition cannot be directly applied to others, largely because predicting atomic arrangements during crystal formation is inherently difficult. Overcoming this challenge is essential to enable rational design and accelerate the synthesis and discovery of new, functionally relevant NMs.

Colloidal chemistry offers a powerful platform for probing reaction kinetics, elucidating mechanisms and tracking intermediate formation, thereby paving the way toward a predictive synthetic framework.[16–22] A promising route toward generalising ABZ nanostructures synthesis is the template approach, in which a binary metal-chalcogenide nanocrystal (NC) or first-generation (G-1) synthon, undergoes partial cation exchange (CE). Here, an additional cation is incorporated *in situ* into the host lattice, enabling the rational construction of a multicomponent structure.[23] While highly promising, this approach has so far been restricted mainly to Cu-chalcogenides,[16] highlighting the need for further exploration to establish a general framework applicable across the broader ABZ material class.

Herein, we report a template-based colloidal synthesis approach for In-based ABZ nanostructures. We demonstrate the first nanoscale synthesis of $NaIn_3Se_5$ and extend the strategy to $NaInS_2$ NCs. We establish the synthetic approach by providing comprehensive mechanistic insights for both systems using X-ray diffraction (XRD), transmission electron microscopy (TEM), and X-ray photoelectron spectroscopy (XPS), and further evaluate their optical properties for potential optoelectronic applications. The combination of precise synthetic control and mechanistic understanding provides a predictive pathway for NC formation in ABZ systems, representing a significant step toward the rational design of functional NMs.

$NaIn_3Se_5$ NCs were prepared using a colloidal hot injection synthesis (see Experimental section for detailed synthesis). XRD analysis confirmed that the NCs are in the trigonal $P(32)$ space group (Fig. 1a and Fig. S1). The experimental peak positions and intensities agree with the $NaIn_3Se_5$ reference pattern (PDF No. 01-071-3539). Rietveld refinement of the experimental pattern yielded cell parameters $a$ = 24.582 Å, $b$ = 24.582 Å, and $c$ = 17.427 Å (Fig. S2). The refinement shows excellent agreement between the experimental data and the reference pattern, with low values of the goodness-of-fit ($\sim$1.14) and the weighted profile residual ($R_{wp}$) ($\sim$7.84), confirming the phase purity. The corresponding crystal structure (Fig. S1b) reveals a complex 3D framework composed of superpolydedral chalcogenide clusters.[24] TEM images reveal a hexagonal nanocuboid like morphology for $NaIn_3Se_5$ NCs (Fig. 1b).

High-resolution TEM (HRTEM) combined with fast Fourier transform (FFT) analysis (Fig. 1c–e) further confirms the formation of the hexagonal crystal structure. The FFT patterns

*Department of Chemical Sciences and Bernal Institute, University of Limerick, V94 T9PX Limerick, Ireland. E-mail: Shalini.Singh@ul.ie, Niraj.Patil@ul.ie*

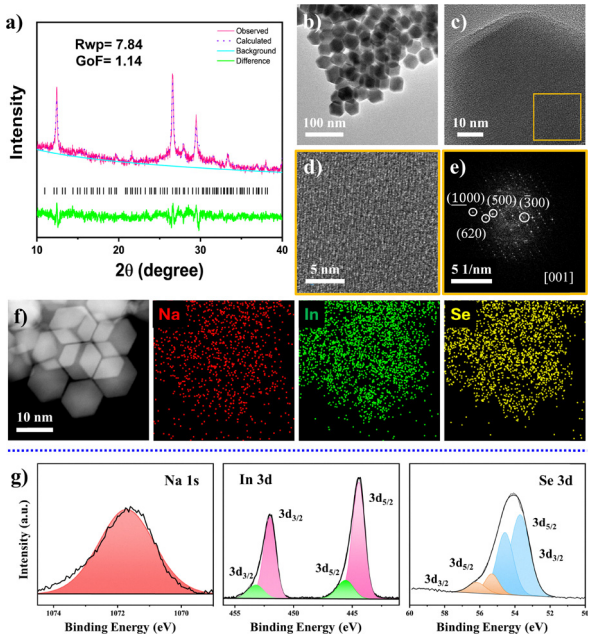


Fig. 1 Structural and compositional analysis of $NaIn_3Se_5$ NCs. (a) XRD analysis using Rietveld refinement, reference pattern PDF No. 01-071-3539. (b) TEM image of $NaIn_3Se_5$ NCs. (c)–(e) High resolution TEM image of $NaIn_3Se_5$ NCs with corresponding FFT pattern. (f) HAADF image and corresponding STEM-EDS maps for Na, In and Se and (g) high resolution XPS spectra of Na, In and Se.

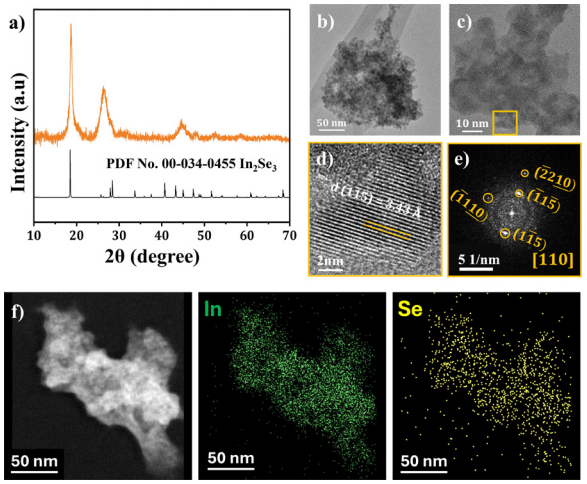


Fig. 2 Analysis of $In_2Se_3$ template formed *in situ* before Na injection (a) XRD analysis. (b) TEM image of $In_2Se_3$ nanoparticles (c) HRTEM image of $In_2Se_3$ nanoparticles (d) and (e) enlarged view of the highlighted area (orange square) in (c) and its FFT showing crystallographic orientation and interplanar distances. (f) HAADF image, and corresponding STEM-EDS maps for In and Se.

display *d*-spacings of ~7.09 Å, 4.26 Å, and 2.95 Å, corresponding to the $(\bar{3}00)$, (500), and (620) planes, respectively. Element maps obtained from scanning transmission electron microscopy with energy dispersive spectroscopy (STEM-EDS) confirmed the simultaneous presence and uniform distribution of Na, In, and Se in the NC (Fig. 1f). XPS was performed to confirm the chemical composition and oxidation states of the NCs (Fig. 1g and Fig. S3). The high-resolution XPS spectra (Fig. 1g) confirm the presence of Na, In and Se as the primary elements of NCs. The Na 1s spectrum (Fig. 1g) shows a peak at ~1071.7 eV, characteristic of the $Na^+$ species. In the In 3d spectra (Fig. 1g), peak fitting reveals a doublet at 444.3 eV and 452.0 eV corresponding to the In $3d_{5/2}$ and $3d_{3/2}$ orbitals in the +3-oxidation state arising from structure. A higher energy doublet at 446.6 eV and 454.5 eV is attributed to oxidised In species.[25] The high-resolution Se 3d spectrum (Fig. 1g) displays two distinct doublets. The first, located at 53.7 eV and 54.6 eV, is assigned to selenide species, while the second doublet at 55.3 eV and 56.2 eV corresponds to surface-oxidised selenium.

The XPS survey spectra (Fig. S3) additionally reveal the presence of C and N, which originate from the surface-bound oleylamine (OLA) ligand. The presence of OLA was further verified by the Fourier transform infrared spectroscopy (FTIR) (Fig. S4), which exhibits characteristic vibrational modes at ~1130 $cm^{-1}$ (C–N stretching), 1600 $cm^{-1}$ (N–H bending), and a broad band at ~3350 $cm^{-1}$ corresponding to the $NH_2$ stretching vibrations.[26] The Raman spectrum of $NaIn_3Se_5$ exhibits two prominent vibrational modes at 160 and 234 $cm^{-1}$, which are associated with the covalently bonded In–Se framework (Fig. S5). The intense peak at 160 $cm^{-1}$ can be assigned to the primary optical $A_1$ symmetric breathing mode of the $[InSe_4]$ tetrahedra similar to indium-selenium ordered-vacancy compounds.[27] The peak at 234 $cm^{-1}$ corresponds to higher-frequency asymmetric stretching vibrations of In–Se bonds.

To elucidate the template formation and reaction pathway leading to $NaIn_3Se_5$ NCs, an aliquot was extracted from the reaction mixture at 260 °C prior to the incorporation of Na precursor in the flask. The structural and morphological evolution of this intermediate was analysed by XRD and TEM (Fig. 2). XRD analysis (Fig. 2a) confirms that the intermediate crystallises as $In_2Se_3$ in the trigonal $R\bar{3}m$ space group. The broad diffraction features indicate a low degree of long-range order, consistent with the formation of very small NCs. The TEM images (Fig. 2b and c) corroborate the presence of small $In_2Se_3$ NCs. HRTEM (Fig. 2c), combined with corresponding FFT analysis (Fig. 2d and e), further confirms the trigonal crystal structure. The FFT pattern displays *d*-spacings of ~3.43 Å which can be indexed to the $(1\bar{1}5)$ plane in close agreement with the reference $In_2Se_3$ structure (PDF: 01-085-9716). And EDS analysis further confirmed the formation of binary $In_2Se_3$ template (Fig. 2f).

The *in situ* formation of this $In_2Se_3$ phase is a critical prerequisite for the subsequent synthesis of $NaIn_3Se_5$, underscoring its role as a structural template. In this template-mediated growth mechanism, the pre-formed indium selenide lattice undergoes atomic reorganisation upon injection of the Na precursor at higher temperature, driving a symmetry reduction from trigonal $R\bar{3}m$ to trigonal $P(32)$ and yielding $NaIn_3Se_5$. Control experiments were conducted to determine the optimal temperature window for $NaIn_3Se_5$ formation (Fig. S6). The phase evolution of Na–In–Se NCs was first examined by XRD as a function of Na-oleate injection temperature. At 220 °C, the XRD pattern exhibits broad and weak spectra, indicating low

crystallinity and incomplete conversion of the binary In–Se template into the ternary Na–In–Se compound (Fig. S6). This is supported by TEM analysis, which shows predominantly small, irregular nanoparticles (NPs) along with hexagonal nanoplate-like crystallites, suggesting heterogeneous growth and incomplete phase transformation (Fig. S7a–e). In contrast, at 300 °C, additional diffraction peaks, indicating the coexistence of $NaIn_3Se_5$ and $NaInSe_2$ ternary phases (Fig. S6). TEM images of this sample reveal two distinct morphologies, NPs and plate-like crystals, further supporting the formation of two crystalline Na–In–Se phases at higher injection temperature (Fig. S7f–i). Overall, these results demonstrate that the Na-oleate injection temperature strongly governs both phase selectivity and morphology, with lower temperature favouring residual binary In–Se, while higher temperature promotes competing ternary Na–In–Se phases. Additionally, to understand the role of the Se precursor and assess the versatility of the synthesis, elemental Se powder was replaced with diphenyldiselenide (DPDSe) and selenourea. XRD analysis confirms the formation of $NaIn_3Se_5$ phase in both cases (Fig. S8). The DPDSe-derived sample shows sharper and more defined peaks, indicating better crystallinity, whereas the selenourea-derived sample exhibits broad and weak peaks, suggesting smaller crystallites. TEM analysis further reveals precursor-dependent morphology. DPDSe produces well-defined, faceted NPs with clear lattice fringes and distinct spots in FFT, confirming good crystallinity (Fig. S9a–d). In contrast, selenourea leads to highly aggregated, smaller particles, indicating rapid nucleation and less controlled growth (Fig. S9e–h). Overall, the Se precursor strongly influences both the crystallinity and morphology of $NaIn_3Se_5$.

To evaluate the generality of the template-mediated synthesis strategy across the ABZ compositional space, we investigated anion substitution at the Z site by replacing selenium with sulfur to access a sulfide-based ternary phase. For this case, of elemental selenium was directly substituted with an amount of elemental sulfur; all other conditions for the synthesis were maintained similar to those for the $NaIn_3Se_5$ NCs synthesis. This controlled substitution enabled us to assess whether template-driven atomic reorganisation can accommodate changes in anion chemistry and local lattice metrics without disrupting the overall crystallographic framework.

Similarly to the trigonal $NaIn_3Se_5$ NCs, phase-pure $NaInS_2$ NCs were obtained after a 60-minute reaction time, indicating that the template-based growth mechanism is robust to chalcogen substitution. Structural characterisation by XRD analysis revealed that the $NaInS_2$ adopts the same trigonal $P(32)$ space group as $NaIn_3Se_5$, suggesting that the underlying framework topology is preserved despite the reduced ionic radius and increased electronegativity of sulfur (Fig. 3a and Fig. S10). Rietveld refinement confirms the phase purity of the NCs, yielding a GOF value of 1.05 and a $R_{wp}$ of 9.24 with refined cell parameters in close agreement with the reference pattern (Fig. 3a and Fig. S11). The crystal structure consists of a 3D network of corner and edge-sharing $NaS_6$ and $InS_6$ octahedra with average Na–S and In–S bond lengths of 2.88 Å and 2.65 Å, respectively, as shown in Fig. S10b.[28] The hexagonal morphology of the NCs is

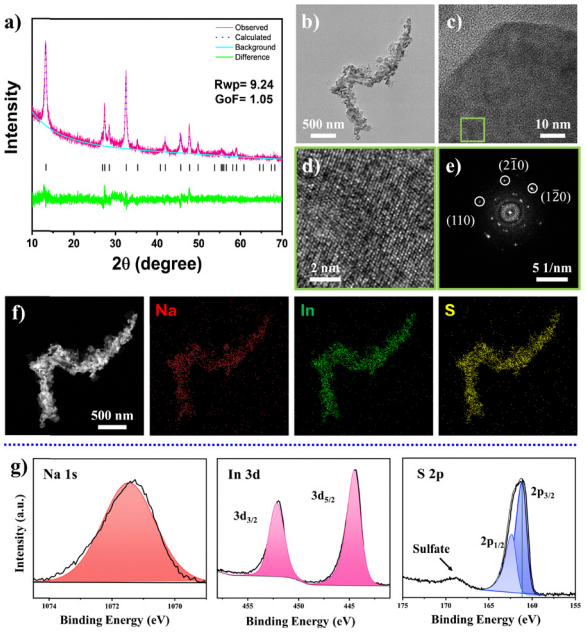


Fig. 3 Structural and compositional analysis of $NaInS_2$ NCs. (a) XRD analysis using Rietveld refinement, reference pattern PDF No. 04-003-9955. (b) TEM image of $NaInS_2$ NCs. (c)–(e) High resolution TEM image of $NaInS_2$ NCs with corresponding fast Fourier transform (FFT) pattern. (f) HAADF image and corresponding STEM-EDS maps for Na, In and S and (g) high resolution XPS spectra of Na, In and S.

displayed in Fig. 3b and c while HRTEM images (Fig. 3d and e) further confirm the formation of $NaInS_2$ NCs through the measured $d$-spacings (~5.21 Å) with the reference values for both the (110) and (2$\bar{1}$0) planes. Elemental mapping by STEM-EDS (Fig. 3f) confirmed the uniform distribution of Na, In and S within the NCs.

To further verify the composition, XPS analysis was performed on $NaInS_2$ NCs. The survey spectra confirmed the presence of Na, In, and S as the primary elements (Fig. S3), which displayed a peak at 444.5 eV, characteristic of the In $3d_{5/2}$ orbital in the +3-oxidation state (Fig. 3g). The S 2p spectrum (Fig. 3g) exhibited doublet at 161.2 eV, consistent with sulfide ($S^{2-}$), and broad peak at 168.7 eV, attributed to surface oxidation forming the sulfate species ($SO_4^{2-}$). The surface functionalities of the synthesised NCs were found to be identical to those of $NaIn_3Se_5$, with OLA acting as a surface-bound ligand (Fig. S12). Raman spectra exhibited characteristic peaks at 160 and 291 $cm^{-1}$, which are consistent with previous reports, further confirming the formation of $NaInS_2$ phase (Fig. S13).[29] Further mechanistic insight was provided by an aliquot study in which the aliquot was extracted prior to Na incorporation during $NaInS_2$ synthesis (Fig. S14), revealing the formation of $In_{1.95}S_3$ as an intermediate phase. This sulfide template reflects on the role of indium selenide in the selenide system and facilitates the subsequent incorporation of Na through atomic rearrangement within the pre-organised indium sulfide lattice, ultimately yielding phase-pure $NaInS_2$. Indium sulphide served as a template, facilitating the growth of phase-pure $NaInS_2$. In analogy to $NaIn_3Se_5$, systematic variations in reaction temperature, reaction

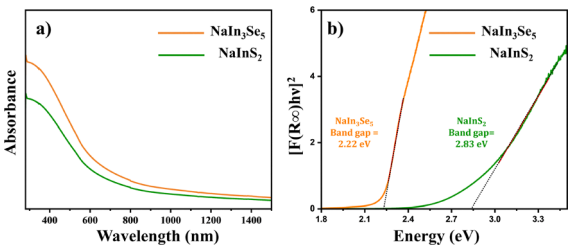


Fig. 4 Optical property analysis. (a) Absorbance spectrum. (b) Tauc plot analysis for for $NaIn_3Se_5$ and $NaInS_2$ NCs.

time, and sulfur precursor were performed for $NaInS_2$ to demonstrate the tunability and general applicability of the synthetic strategy (detailed info in SI section S2.11). This observation of indium chalcogenide templates across both Se and S validates that ABZ NCs form *via* an *in situ* developed template-based approach rather than direct ternary nucleation.

Finally, we studied the optical behaviour of $NaIn_3Se_5$ NCs and $NaInS_2$ NCs using UV-vis-NIR absorption and diffuse reflectance spectroscopy. Both NCs show strong absorption in the UV-vis region with absorption onset around the NIR region, as shown in Fig. 4a. The optical band gaps were estimated using Tauc plots derived from reflectance spectra of $NaIn_3Se_5$ NCs and $NaInS_2$ NCs. The experimentally measured band gaps of 2.22 eV and 2.83 eV for $NaInS_2$ NCs and $NaIn_3Se_5$ NCs, respectively (Fig. 4b), are consistent with the previous computational reports.[30–33] With these optimal band gaps and significant absorption characteristics, $NaIn_3Se_5$ and $NaInS_2$ NCs can be promising materials for photocatalysis, tandem solar cell absorbers, and photodetectors.[24]

In summary, we have overcome a critical challenge in the synthesis of ternary alkali metal chalcogenides by developing a facile template-based strategy. This approach relies on a metal chalcogenide synthon to effectively direct phase evolution and guide the formation of the desired nanocrystalline $NaIn_3Se_5$ structure. The versatility of the method was further demonstrated in the sulfide system, underscoring its broader applicability. We also display the relationship between the binary synthon and the resulting ternary crystal phase. The successful extension from selenide to sulfide systems demonstrates the generalizability of this synthetic strategy, suggesting its potential applicability to other systems containing different alkali metals such as Li or K, or alternative metal centers such as Ga through suitable selection of metal and chalcogen precursors. Extending this strategy to other alkali metals may enable streamlined discovery and provide new opportunities for the targeted design of functional ABZ NMs for energy applications.

## Conflicts of interest

There are no conflicts to declare.

## Data availability

The data that support the findings of this study are available on request from the corresponding author.

Supplementary information (SI): includes materials and methods for synthesis of nanostructures with extra data regarding: (i) XRD analysis, (ii) refinement Parameters for Se and S systems (iii) STEM-EDS data (iv) XPS spectra (v) control experiments (vi) XRD, TEM and STEM EDS for aliquots. See DOI: https://doi.org/10.1039/d6cc01363e.

## Acknowledgements

This publication has emanated from research conducted with the financial support of Taighde Éireann – Research Ireland under Grant number 22/FFP-P/11591. H.M. acknowledges funding from the Research Ireland centre MaREI. M.A. acknowledges funding from Research Ireland fellowship GOIPD/2025/1538.

## References

1 C. Q. Li and J. J. Wang, *Small*, 2024, **20**, 2404798.
2 Y. Zhang, Y. Huang, S. S. Zhu, Y. Y. Liu, X. Zhang, J. J. Wang and A. Braun, *Small*, 2021, **17**, 2100320.
3 N. N. Patil, R. Wu, C. Fiedler, N. Kapuria, B. Nan, N. Jakhar, A. Cabot, M. Ibáñez, K. M. Ryan, A. M. Ganose and S. Singh, *ACS Energy Lett.*, 2026, **11**, 481–488.
4 H. McKeever, N. Kapuria, A. Nicolson, S. Sen, D. Scanlon, K. M. Ryan and S. Singh, *Nano Lett.*, 2025, **25**, 4652–4658.
5 H. McKeever, N. N. Patil, M. Palabathuni and S. Singh, *Chem. Mater.*, 2023, **35**, 9833–9846.
6 N. Kapuria, B. Nan, T. E. Adegoke, U. Bangert, A. Cabot, S. Singh and K. M. Ryan, *Chem. Mater.*, 2023, **35**, 4810–4820.
7 A. M. Medina-Gonzalez, P. Yox, Y. Chen, M. A. S. Adamson, B. A. Rosales, M. Svay, E. A. Smith, R. D. Schaller, K. Wu, A. J. Rossini, K. Kovnir and J. Vela, *Chem. Mater.*, 2022, **34**, 7357–7368.
8 Y.-T. Huang, S. R. Kavanagh, D. O. Scanlon, A. Walsh and R. L. Z. Hoye, *Nanotechnology*, 2021, **32**, 132004.
9 Z. Sun, N. Pham, S. Derakhshan and R. L. Brutchey, *Chem. Sci.*, 2025, **16**, 18722–18728.
10 M. Bouchenafa, Y. Bourourou, A. Khelefhoum, H. Boulebda, M. A. Fadla, A. Benmakhlouf, S. Maabed, M. Halit and M. Sidoumou, *Comput. Condens. Matter*, 2022, **30**, 00644.
11 A. Banerjee, K. H. Park, J. W. Heo, Y. J. Nam, C. K. Moon, S. M. Oh, S. T. Hong and Y. S. Jung, *Angew. Chem.*, 2016, **128**, 9786–9790.
12 N. Ma, Y.-Y. Li, L. Chen and L.-M. Wu, *J. Am. Chem. Soc.*, 2020, **142**, 5293–5303.
13 Y. Chen, Y. Shen, X. Li, J. Sun and Q. Wang, *Adv. Theory Simul.*, 2020, **3**, 2000169.
14 Z. Xia, H. Fang, X. Zhang, M. S. Molokeev, R. Gautier, Q. Yan, S.-H. Wei and K. R. Poeppelmeier, *Chem. Mater.*, 2018, **30**, 1121–1126.
15 M. M. Hossain, M. A. Ali, M. M. Uddin, M. A. Hossain, M. Rasadujjaman, S. H. Naqib, M. Nagao, S. Watauchi and I. Tanaka, *Mater. Today Commun.*, 2021, **26**, 101988.
16 N. Kapuria, N. N. Patil, K. M. Ryan and S. Singh, *Nanoscale*, 2022, **14**, 2885–2914.
17 N. Kapuria, N. N. Patil, A. Sankaran, F. Laffir, H. Geaney, E. Magner, M. Scanlon, K. M. Ryan and S. Singh, *J. Mater. Chem. A*, 2023, **11**, 11341–11353.
18 M. Mishra, N. N. Patil, M. Zubair, N. Kapuria, V. Lebedev, T. E. Adegoke, K. M. Ryan and S. Singh, *Nanotechnology*, 2022, **33**, 305602.
19 N. N. Patil, A. Sankaran, T. E. Adegoke, K. M. Ryan and S. Singh, *Small Struct.*, 2025, **6**, 2500159.
20 S. Sen, N. N. Patil, A. Bora, M. Palabathuni, T. E. Adegoke, K. M. Ryan, K. Rossi and S. Singh, *Nano Lett.*, 2025, **25**, 12207–12215.
21 A. Loiudice and R. Buonsanti, *Nat. Synth.*, 2022, **1**, 344–351.
22 M. Ibáñez, S. C. Boehme, R. Buonsanti, J. De Roo, D. J. Milliron, S. Ithurria, A. L. Rogach, A. Cabot, M. Yarema, B. M. Cossairt, P. Reiss, D. V. Talapin, L. Protesescu, Z. Hens, I. Infante, M. I. Bodnarchuk, X. Ye, Y. Wang, H. Zhang, E. Lhuillier,

V. I. Klimov, H. Utzat, G. Rainò, C. R. Kagan, M. Cargnello, J. S. Son and M. V. Kovalenko, *ACS Nano*, 2025, **19**, 31969–32051.
23 Q. A. Akkerman, A. Genovese, C. George, M. Prato, I. Moreels, A. Casu, S. Marras, A. Curcio, A. Scarpellini, T. Pellegrino, L. Manna and V. Lesnyak, *ACS Nano*, 2015, **9**, 521–531.
24 S.-F. Li, X.-M. Jiang, B.-W. Liu, D. Yan, C.-S. Lin, H.-Y. Zeng and G.-C. Guo, *Chem. Mater.*, 2017, **29**, 1796–1804.
25 S.-W. Hsiao, C.-S. Yang, H.-N. Yang, C.-H. Wu, S.-K. Wu, L.-Y. Chang, Y.-T. Ho, S.-J. Chang and W.-C. Chou, *Front. Mater.*, 2022, **9**, 871003.
26 A. N. Roth, Y. Chen, M. A. S. Adamson, E. Gi, M. Wagner, A. J. Rossini and J. Vela, *ACS Nano*, 2022, **16**, 12024–12035.
27 R. Vilaplana, S. G. Parra, A. Jorge-Montero, P. Rodríguez-Hernández, A. Munoz, D. Errandonea, A. Segura and F. J. Manjón, *Inorg. Chem.*, 2018, **57**, 8241–8252.
28 A. Jain, S. P. Ong, G. Hautier, W. Chen, W. D. Richards, S. Dacek, S. Cholia, D. Gunter, D. Skinner, G. Ceder and K. A. Persson, *APL Mater.*, 2013, **1**, 011002.
29 J. K. Larsen, K. V. Sopiha, C. Persson, C. Platzer-Bjorkman and M. Edoff, *Adv. Sci.*, 2022, **9**, 2200848.
30 M. M. Hossain, M. A. Hossain, S. A. Moon, M. A. Ali, M. M. Uddin, S. H. Naqib, A. K. M. A. Islam, M. Nagao, S. Watauchi and I. Tanaka, *J. Mater. Sci.: Mater. Electron.*, 2021, **32**, 3878–3893.
31 Y. Fu, X. Duan, M. Xing, N. Zhang, X. Luo, H. Wang and Y. Ma, *Mater. Lett.*, 2014, **12**, 141–143.
32 A. Kudo, A. Nagane, I. Tsuji and H. Kato, *Chem. Lett.*, 2002, 882–883.
33 N. Takahashi, H. Ito, A. Miura, N. C. Rosero-Navarro, Y. Goto, Y. Mizuguchi, C. Moriyoshi, Y. Kuroiwa, M. Nagao, S. Watauchi, I. Tanaka and K. Tadanaga, *J. Alloys Compd.*, 2018, **750**, 409–413.